

# Nanoscale

Accepted Manuscript



This is an *Accepted Manuscript*, which has been through the Royal Society of Chemistry peer review process and has been accepted for publication.

*Accepted Manuscripts* are published online shortly after acceptance, before technical editing, formatting and proof reading. Using this free service, authors can make their results available to the community, in citable form, before we publish the edited article. We will replace this *Accepted Manuscript* with the edited and formatted *Advance Article* as soon as it is available.

You can find more information about *Accepted Manuscripts* in the [Information for Authors](#).

Please note that technical editing may introduce minor changes to the text and/or graphics, which may alter content. The journal's standard [Terms & Conditions](#) and the [Ethical guidelines](#) still apply. In no event shall the Royal Society of Chemistry be held responsible for any errors or omissions in this *Accepted Manuscript* or any consequences arising from the use of any information it contains.

# Massive Production of Graphene Nanoscrolls and Their Assist for High Rate Performance Supercapacitors

Bingna Zheng, Zhen Xu, Chao Gao\*

MOE Key Laboratory of Macromolecular Synthesis and Functionalization, Department of Polymer Science and Engineering, Zhejiang University, 38 Zheda Road, Hangzhou 310027, P. R. China.

\* To whom correspondence should be addressed. E-mail: [chaogao@zju.edu.cn](mailto:chaogao@zju.edu.cn)

## Abstract

The output of graphene nanoscrolls (GNSs) has been greatly enhanced to gram-level by improved spray-freezing drying method without damaging the high transforming efficiency (>92%). The lowest bulk density of GNS foam reaches 0.10 mg/cm<sup>3</sup>. Due to the unique morphology and high specific surface area (386.4 m<sup>2</sup>/g), the specific capacitances of GNSs (90-100 F/g at 1 A/g) are all superior to those of multiwall carbon nanotubes meanwhile holding the excellent rate capabilities (60-80% retention at 50 A/g). For the first time, all-graphene-based films (AGFs) are fabricated via the intercalation of GNSs into graphene layers. AGF exhibits a capacitance of 166.8 F/g at 1 A/g and rate capability (83.9% retention at 50 A/g) better than pure reduced graphene oxide (RGO) films and carbon nanotubes/graphene hybrid films (CGFs).

## 1. Introduction

Graphene nanoscrolls (GNSs) have drawn an increasing attention to researchers recently due to their unique one-dimensional tubular topology.<sup>1-27</sup> The open structure of GNS enables a more efficient utilization of the surface area of graphene sheets and inherits the morphology advantages of traditional carbon nanotubes (CNT). The above specialties provide GNS with abundant applications like hydrogen storage,<sup>28-30</sup> supercapacitors,<sup>5, 18, 21, 24</sup> batteries,<sup>14, 23</sup> sensors<sup>12</sup> and electronic devices<sup>11, 19</sup>.

The fabrication history of GNS has experienced the period from high energy consuming, low yields to the facile, environment green ways. Besides, the conflict between high quality and large quantity is still an unsolved issue. Harsh reaction condition like ultra-active metal intercalation<sup>1</sup> and bottom-up high temperature synthesis<sup>4, 7</sup> are not suitable for massive production. The methods that make use of the interface forces, such as surface strain,<sup>3, 5</sup> Langmuir-Blodgett compression,<sup>13</sup> capillary reaction<sup>25</sup> and molecular combing,<sup>12</sup> all give rise to the high quality GNSs with tiny amount. Nanoparticle template-induced formation is another major technique and has larger output than the above ones. Sharifi et al reported the reversible formation of GNS with the help of magnetic  $\gamma$ -Fe<sub>2</sub>O<sub>3</sub> nanoparticles, which also means the instability of pristine GNS.<sup>11</sup> Mai and his group members designed the semi hollow bicontinuous GNS with V<sub>3</sub>O<sub>7</sub> or MnO<sub>2</sub> templates, which have enhanced energy storage performances.<sup>14</sup> Other templates such as carbon nanotubes,<sup>15</sup> TiO<sub>2</sub>,<sup>23</sup> Co<sub>3</sub>O<sub>4</sub>,<sup>24</sup> Fe<sub>3</sub>O<sub>4</sub> and Ag<sup>17</sup> have also been reported. The cost and removal difficulty of templates are their main hindrance to large scale production and applications.

Recently, our group has reported the high efficient synthesis of GNS by well-controlled lyophilization.<sup>31</sup> The main factors including freezing speed, reduction degree and solution concentration that affect GNS transformation have also been revealed. Enlightened by the mechanism, here we have reformed our former production method by spray-freezing method to reduce the size of liquid drops, which ensures the fast freezing speed of samples. The output has been enhanced to gram-level by increasing of the feeding GO dispersion without damaging the transforming efficiency (>92%). The density of the obtained GNS can be regulated flexibly from 0.1 to 0.5 mg/cm<sup>3</sup>. Based on a 3D framework constituted by scrolls of giant graphene sheets, the density can be as low as ~0.10 mg/cm<sup>3</sup>. This value is lower than world's lightest solid material (0.12 mg/cm<sup>3</sup>).<sup>32, 33</sup> Moreover, the high density GNS enables quantity-costing characterizations like Brunauer-Emmett-Teller (BET) which has not been given in vast majority of GNS related papers. The specific surface area (SSA) of GNS reaches 386.4 m<sup>2</sup>/g, the highest value among the reported GNS materials.

Given the intrinsic graphene nature with large surface area and good electrical conductivity, GNS is supposed to have similar energy storage performance as graphene. Due to the one-dimensional CNT-like nanostructure and unique swelling behavior,<sup>31</sup> GNS will avoid sheets restacking and may have better rate performance than pure graphene. GNS-based supercapacitors in previous reports mainly exhibit good performance as we predicted but the rate performances were scarcely mentioned. Here, we have discovered the better specific capacitances of GNSs (90-100 F/g at 1

A/g) than multiwall carbon nanotubes (MWNTs) (~ 40 F/g at 1 A/g) without sacrificing the rate capabilities of GNSs (60-80% rate retention at 50 A/g). Due to the ascendant electrochemical performance and characteristic reversible swelling behavior,<sup>26, 27, 31</sup> we have prepared all-graphene-based films (AGFs) by adding GNS into graphene oxide followed by solution casting. The best specific capacitance of AGFs reached 166.8 F/g at 1 A/g and reserved 83.9% (140 F/g) at 50 A/g, which performs better than carbon nanotubes/graphene hybrid films (CGFs) and RGO films. The excellent performance of AGFs guarantees facile incorporation with other guest materials and large scale application in film supercapacitors with high specific capacitance and rate capability.

## 2. Experimental Section

### 2.1 Materials

Ultra large single-layer graphene oxide (#GO-3) (Average sheet size: ~71  $\mu\text{m}$ ; Thickness: 0.8-1.0 nm; Polydispersity: 0.45) was purchased from C6G6 (www.c6g6.com). Multiwall carbon nanotubes (OD>50nm, 95%) were bought from Chengdu Institute of Organic Chemicals Co., Ltd. 85%  $\text{N}_2\text{H}_4 \cdot \text{H}_2\text{O}$  solution, ethanol, dimethylformamide (DMF), acetonitrile (AN), were obtained from Sinopharm Chemical Reagent Co., Ltd and used as received. 1-ethyl-3-methylimidazolium tetrafluoroborate ( $\text{EMIM}^+ \text{BF}_4^-$ ) was purchased from Aladdin Industrial Inc.

### 2.2 Characterizations

SEM images were taken on a Hitachi S4800 field-emission SEM system. BET surface area measurement is conducted by the Quantachrome instrument (Autosorb-1-C). XRD data were collected with a D/MAX-MB diffractometer using monochromatic Cu K $\alpha$ 1 radiation ( $\lambda = 1.5406 \text{ \AA}$ ) at 40 kV 250 mA. Raman measurements were conducted on inVia-Reflex. Electrochemical impedance spectroscopy (EIS), cyclic voltammetry (CV) and galvanostatic charge-discharge (GCD) measurements were performed using an electrochemical workstation (CHI 660e, CH Instruments, Inc.). Cycling performance test was conducted by CT2001A small current battery testing system.

### 2.3 Preparation of GNSs

The giant graphene oxide (GGO) was purchased from C6G6 and the synthesis method is based on the modified Hummers' method previously reported by our group.<sup>34-37</sup> The initial GGO aqueous dispersions were from 0.01 mg/mL to 0.5 mg/mL. N<sub>2</sub>H<sub>4</sub>·H<sub>2</sub>O solution was added dropwise into GGO dispersions (weight ratio of 85% N<sub>2</sub>H<sub>4</sub>·H<sub>2</sub>O solution to GGO was about 15:1) followed by 5 min magnetic stirring. The above GGO dispersions were transformed into chemical reduced graphene (CRG) by transferring to 60 °C oil bath and kept for 30 min with stirring. CRG dispersions were sprayed into liquid nitrogen bath with the product of grey colored ice particles (Figure 1A). The ice particles were freezing dried in lyophilizer with an optimized temperature programme and GNSs with low reduction degree were obtained. The low reduction degree GNSs were kept in a sealed container with N<sub>2</sub>H<sub>4</sub> at 90 °C for 12 h to

obtain GNSs.

#### 2.4 Preparation of AGFs and CGFs

GNSs were dispersed in DMF with ultrasonic cell disruptor for 10 s at 480 W, resulting a 2 mg/mL dispersion. Different amount of GNS dispersion was added into 20 mg/mL GO/DMF dispersion resulting GNS/GO suspensions (weight ratio of GNS: GO ranges from 5:95 to 15:85, final concentration of GO solution was 7~8 mg/mL). MWNT/GO suspensions were prepared by the same procedure as GNS/GO. The above suspensions were directly poured on PTFE boards and knocked on the desk for several times to remove bubbles. After that, the boards were placed in the oven horizontally and kept at 50 °C for 12h to evaporate most of the DMF. Then, the half-dried films were peeled off the substrate by soaking with ethanol. The peeled-off films were immersed in 90 °C  $\text{N}_2\text{H}_4\cdot\text{H}_2\text{O}$ /ethanol/water mixed solution (0.75 mg/mL  $\text{N}_2\text{H}_4\cdot\text{H}_2\text{O}$ ) for 12h, resulting AGFs and CGFs. For the wet films, ethanol is exchanged by electrolytes (1M  $\text{H}_2\text{SO}_4$  or 1M ( $\text{EMIM}^+ \text{BF}_4^-$ ) in acetonitrile) before using. For the dry films, ethanol is evaporated before using. With the different guest materials, AGFs are named as AGF1 (GNS: GO=5:95), AGF2 (GNS: GO=10:90) and AGF3 (GNS: GO=15:85), respectively. Similarly, CGFs are named as CGF1, CGF2 and CGF3, respectively. For electrochemical tests, all the above films were cut into round shapes and sealed into a detachable stainless steel cell (custom-made from Institute of Physics CAS) with mixed cellulose acetate ester membrane (aqueous

electrolyte) or Nylon membrane (organic electrolyte) as a separator (purchased from Yaxing Purification Materials Factory,  $\Phi=0.45\ \mu\text{m}$ ).

### **3. Results and discussion**

#### **3.1 Massive production of GNS**

The main factors that affect GNS transformation efficiency include the freezing speed, reduction degree of GGO and concentration of GGO solution which were systematically studied by our group. The three factors interact with each other: with the increase of GGO reduction degree and solution concentration, the freezing speed should be elevated, correspondingly. In the light of this mechanism, massive production of GNS can be realized by changing the freezing speed. The bulk freezing method was changed by spray-freezing method. Here, GNSs with different initial concentrations of GGO solutions (0.01, 0.05, 0.1, 0.2, 0.5 mg/ml) are named as GNS1 to GNS5, respectively. As shown in Figure 1A, CRG solution is sprayed into liquid nitrogen bath through a tailored spray head. Due to the shrink of drop size, the freezing rate has been significantly increased than a large piece of ice. As shown in Figure 1B and C, 150 mL GNS foam with 0.5 mg/ml density was fabricated and the transforming efficiency is above 92% (Figure S1). The similar scroll-like morphology (Figure 1D and E) was also obtained. Moreover, due to the increase of concentration, some GNS bundles also exist.

#### **3.2 Low density of GNS foam**

The bulk density of GNS can be regulated flexibly from a relatively high value to a very low limit. The physical entanglements of one-dimensional (1D) scrolls and intrinsic elastic force of graphene sheets result the three-dimensional (3D) framework of GNS foam. The lowest bulk density achieved by experiment is as low as 0.10 mg/mL (Figure 1F, Figure S2), which is among the lowest density of solid materials. A very simple geometric model for density calculation is proposed in Figure S2. The calculated density of GNS foam  $\rho=6/(S*h)$  (where  $S$  denotes the specific surface area and  $h$  represents the average length of GNS. More details of this modeling are shown in supporting information). The calculated lowest bulk density of GNS is 0.032 mg/mL, when  $S$  is the ideal value of graphene ( $2630 \text{ m}^2/\text{g}$ ) and  $h$  is the average lateral width of our GGO ( $71\mu\text{m}$ ). For the typical case of GNS5 ( $h=10\sim 20\mu\text{m}$  observed by SEM), the calculated density of GNS5 is 0.112~0.227 mg/mL, which is closed to our experimental value. This simple model clearly demonstrates that the larger of the GNS length and specific surface area, the lower of the bulk density. With the decrease of density, the networks of GNS can be seen by naked eyes (Figure S3). The flyweight GNS foam can stand on a piece of cotton without deforming it (Figure 1G).

### 3.3 Characterizations of GNS

Massive production of GNS is crucial to its characterization and application. Limited by the low output, only a few groups have reported the specific surface area of GNS.<sup>5, 9, 23</sup> Here, we have solved the massive production of GNS and obtained the highest specific surface area of GNS ever reported. The nitrogen

adsorption/desorption isotherms shown in Figure 2A indicates GNS5 has an interconnected pore system with the characteristic IUPAC H2 hysteresis.<sup>45</sup> The low pressure region ( $P/P_0=0\sim 0.1$ ) reflects the strong adsorption affinity for the micro-pores and nitrogen. At the medium pressure region ( $P/P_0=0.3\sim 0.8$ ), the linear plots reveal the nitrogen condensation in meso-pores. Based on the linear relative pressure range 0.1~0.3, the calculated SSA is 386.4 m<sup>2</sup>/g. Figure 2B shows the well-defined pore volume and pore size distribution of GNS based on the quenched solid state density function theory (QSDFT). The cumulative pore volume reaches to 0.5 cm<sup>3</sup>/g. The micro-pores mostly centralized in a narrow size range of ~0.7nm. The meso-pores are mainly distributed at 2.7 nm size.

As to the large SSA and unique structure, we test the electrochemical performances of GNSs. Figure 2C and 2D reflect good electrochemical double layer capacitance (EDLC) performance with the rectangular shape CV curves and triangle GCD curves. The specific capacitances ( $C_s$ ) of GNSs are in the range of 90-100 F/g at 10 mV/s and show 45-60% retention at 2 V/s (Table S1). The retention rates are as good as MWNTs (42.5%) with a twice larger  $C_s$  than MWNTs (46.7 F/g). Same tendencies are also found in GCD tests (Table S2) and the retention rates are in the range of 60-80%. The high specific capacitance and rate performance can be ascribed to the characteristic nano-structures of GNS. The scrolled morphology provides large SSA which is beneficial to higher specific capacitances. Furthermore, unlike graphene sheets, the tube-like morphology prevents self-aggregation and is beneficial to fast transportation of electrolytes. Moreover, the special behavior of reversible swelling in

electrolytes has not been found in the seamless concentric structure MWNTs. The performances further prove that GNS is an ideal alternative of MWNT in supercapacitors.

### 3.4 Electrochemical performance of GNS-based films

Graphene-based films are main candidate materials of supercapacitors originating from the excellent EDLC behavior, facile incorporation with other particles and the capability of flexible electrodes.<sup>38-40</sup> Nevertheless, the assembly of graphene usually leads to restacking of graphene sheets, which hinders the performance of macroscopic graphene-based materials. Many efforts have been spent to prevent the restacking and improve the electrochemical performances, such as introducing separating guests (like carbon nanotubes,<sup>41</sup> nano-particles<sup>42-44,48</sup> and electrolyte molecules<sup>50,52</sup>), wrinkled or vertically oriented structures<sup>49,51,53,54</sup> and pores<sup>45</sup> to the systems. Here, with the assist of GNSs which can act as spacer, the interlayer space of graphene sheets is expanded and the swelling behavior further promotes the interlayer space enlarging process. The enlargement of interspace greatly enhanced the rate capability of graphene films.

As shown in Figure 3A, the typical axisymmetric and rectangular CV curves prove the good EDLC property of AGF3. Similar performances can also be observed in other AGF samples (Figure S4). The rectangular shape deterioration trends of AGFs are slower than RGO film and CGFs (Figure S5). The  $C_s$  of AGF3 calculated from GCD method is 166.8 F/g at 1 A/g (Figure 3B). With the increase of current density to

50 A/g, 83.9% ( $C_s = 140.0$  F/g)  $C_s$  retention can be observed (Figure 3C). The specific capacitance of AGF1 at 1 A/g and 50 A/g are 150.0 F/g and 133.4 F/g, respectively. The corresponding capacitance retention is 88.9%. For AGF2, 82.9% capacitance retention is obtained from 1 A/g (152.5 F/g) to 50 A/g (126.5 F/g). For CGF1 to CGF3, 16~50% capacitance retentions are observed from 1 A/g (98.1 F/g, 113.4 F/g and 108.0 F/g, respectively) to 50 A/g (16.3 F/g, 54.2 F/g and 41.5 F/g, respectively). The retention rates of RGO film from 1 A/g (115.7 F/g) to 50 A/g (61.0 F/g) is 52.7%. It is obvious that the performances of AGFs are all superior to RGO and CGFs. Compared with other related high rate capability works (Figure 3D and E), AGFs have relatively high  $C_s$  as well as capacitance retentions at extremely high current density (77.4% at 100 A/g). The Ragone plots of RGO, AGF3, CGF3, GNS and MWNTs were shown in Figure S6. Both the energy density and power density are better than other control samples.

The electrochemical impedance spectroscopy (EIS) was conducted from 0.01 Hz to 100 kHz, which further confirmed the fast ion transport of AGFs (Figure 3F). Compared with the relatively compact morphology of RGO and CGF3, fluffy morphology of AGF3 leads to lower electric conductivity and larger equivalent series resistances (ESR) of AGF3. However, within the testing frequency range, Nyquist plot of AGF3 is more vertical to the axis than RGO and CGF3, demonstrating the ideal EDLC behavior. At the high frequency range, the semi-circle of AGF3 is negligible comparing with RGO film and CGF3, proving the small charge-transport resistance and interfacial resistance. The characteristic frequencies at  $-45^\circ$  of the three

samples are 0.15 Hz, 2.61 Hz and 0.68 Hz for RGO film, AGF3 and CGF3, respectively (Figure S7). The higher frequency means a better power capability.<sup>38, 45,</sup>

46

For the organic electrolyte system, AGFs have also showed their advantages (Table S3, S4). With the addition of GNSs,  $C_s$  of RGO film at 1 A/g increased from 100.9 F/g to 122.2 F/g. The retention rate from 1 A/g to 20 A/g is 3.9% for AGF3, much better than RGO film (0.001%). The cycling stability has also been investigated and 104.4% initial capacitance was reserved in aqueous electrolyte at 5 A/g (Figure S8).

The reason for the better performance of AGFs than CGFs can be ascribed to the reversible swelling behavior of GNSs. GNSs act as reversible elastic spacers that increase the interspace among the graphene sheets. When immersed in electrolytes, the film will be further swollen, beneficial to the ion transportation. As shown in Figure 4A-C, with the same feed quantity of GO, GNS and MWNTs, the thickness of AGF3 is obviously larger than RGO film and CGF3. More details of the morphologies are shown in Figure S9. The imitation cartoons (Figure 4D-F) express the morphologies of the three kinds of films.

XRD is provided to further prove the intercalation and swollen behavior (Figure 5A and 5B). The characteristic Peak 1 at around 22-24° that attributes to reduced graphene oxide can be observed for all the graphene-based films. Aside from peak 1, a new shoulder Peak 2 at around 15-18° appears.<sup>47</sup> The arise of Peak 2 is ascribe to the half-dried film making method that gives rise to residue solvent among the interlayer. According to Bragg Equation, the d-space of both Peak 1 and Peak 2 are given in

Table 1. The expansions of inter-layer distance for AGFs are larger than CGFs. Moreover, to evaluate the swollen behavior, XRD of electrolyte-soaked films were also tested. As shown in Figure 5B, Peak 2 shift to smaller angles. AGF3 shifted to a  $7.4^\circ$ , which means a larger d-space ( $11.9 \text{ \AA}$ ) was achieved than other samples ( $9.17 \text{ \AA}$  for RGO,  $9.7 \text{ \AA}$  for CGF3).

Figure 5C show the Raman spectra of RGO, AGF3, CGF3 and GO film. D band is obviously stronger than G band in GO film. After reduction, the intensity of D band in all the reduced graphene-based films becomes weaker than that of G band, indicating the structure restoration in the chemical reduction process. This suggests that the emergence of Peak 2 is due to the half-dried film making procedure rather than the existence of GO.

#### 4. Conclusions

The production method of GNS has been reformed by spray freezing drying and the density of GNS foam can be regulated from 0.1-0.5 mg/ml, which can meet different demands of applications. The lowest bulk density of GNS foam ( $0.1 \text{ mg/mL}$ ) is comparable to the lightest solid material ever reported. The high density GNS helps to realize large scale characterizations and applications. The SSA of GNS is  $386.4 \text{ m}^2/\text{g}$ , which exceed the ever reported value. The micro-pore and meso-pore distributions are at  $\sim 0.7 \text{ nm}$  and  $\sim 2.7 \text{ nm}$ , respectively. With the special 1D scrolled open morphology, the specific capacitance ( $90\text{-}100 \text{ F/g}$  at  $10 \text{ mV/s}$ ) is larger than MWNTs along with a same level of rate capability ( $45\text{-}60\%$  at  $2 \text{ V/s}$ ). With the addition of GNS into GO, we

have produced the all-graphene films with the enhanced electrochemical rate performances. The specific capacitance reaches 166.8 F/g at 1 A/g and 83.9% of initial capacitance (140 F/g) is obtained at 50 A/g. The better rate performance than RGO and CGF is mainly caused by the intercalation and swelling behavior of GNS that induce larger expansion of inter-layer space. The facile preparation and excellent electrochemical performance promise AGFs to be applied in real high power density devices.

### **Acknowledgments**

This work is supported by the National Natural Science Foundation of China (No.s 21325417, 51173162 and 5153000079) and State Key Laboratory for Modification of Chemical Fibers and Polymer Materials, Donghua University (no. LK1403).

### **Supporting Information Available**

SEM image for GNS transformation efficiency assessment, images for GNS density modeling and calculation, tables for GNS specific capacitance and retention, figures and tables for AGF, CGF and RGO electrochemical performance comparisons, cycling stability and detailed SEM images of AGF and CGF are available in the supporting information.

### **Reference**

1. L. M. Viculis, J. J. Mack and R. B. Kaner, *Science*, 2003, **299**, 1361.

2. M. Quintana, M. Gizelcazk, K. Spyrou, M. Calvaresi, S. Bals, B. Kooi, G. V. Tendeloo, P. Rudolf, F. Zerbetto and M. Prato, *J. Am. Chem. Soc.*, 2012, **134**, 13310.
3. X. Xie, L. Ju, X. Feng, Y. Sun, R. Zhou, K. Liu, S. Fan, Q. Li and K. Jiang, *Nano Lett.*, 2009, **9**, 2565.
4. A. K. Schaper, M. S. Wang, Z. Xu, Y. Bando and D. Golberg, *Nano Lett.*, 2011, **11**, 3295.
5. F. Zeng, Y. Kuang, Y. Wang, Z. Huang, C. Fu and H. Zhou, *Adv. Mater.*, 2011, **23**, 4929.
6. J. Zheng, H. Liu, B. Wu, Y. Guo, T. Wu, G. Yu, Y. Liu and D. Zhu, *Adv. Mater.*, 2011, **23**, 2460.
7. X. Chen, L. Li, X. Sun, H. G. Kia and H. Peng, *Nanotechnology*, 2012, **23**, 055603.
8. Z. Zhang, Y. Huang and T. Li, *J. Appl. Phys.*, 2012, **112**, 063515.
9. P. Yadav, S. Warule, J. Jog and S. Ogale, *Solid State Commun.*, 2012, **152**, 2092.
10. D. Xia, Q. Xue, J. Xie, H. Chen and C. Lv, *Small*, 2010, **6**, 2010.
11. T. Sharifi, E. Gracia-Espino, H. R. Barzegar, X. Jia, F. Nitze, G. Hu, P. Nordblad, C. Tai and T. Wågberg, *Nat. Commun.*, 2013, **4**:2319.
12. H. Li, J. Wu, X. Qi, Q. He, C. Liusman, G. Lu, X. Zhou and H. Zhang, *Small*, 2013, **9**, 382.
13. Y. Gao, X. Chen, H. Xu, Y. Zou, R. Gu, M. Xu, A. K.-Y. Jen and H. Chen, *Carbon*, 2010, **48**, 4475.
14. M. Yan, F. Wang, C. Han, X. Ma, X. Xu, Q. An, L. Xu, C. Niu, Y. Zhao, X. Tian, P. Hu, H. Wu and L. Mai, *J. Am. Chem. Soc.*, 2013, **135**, 18176.
15. Y. Kim and D. Min, *Carbon*, 2010, **48**, 4283.

16. Q. Li, Z. Li, M. Chen and Y. Fang, *Nano Lett.*, 2009, **9**, 2129.
17. X. Wang, D. Yang, G. Huang, P. Huang, G. Shen, S. Guo, Y. Mei and D. Cui, *J. Mater. Chem.*, 2012, **22**, 17441.
18. F. Zeng, Y. Kuang, G. Liu, R. Liu, Z. Huang, C. Fu and H. Zhou, *Nanoscale*, 2012, **4**, 3997.
19. K. Feng, B. Tang and P. Wu, *ACS Appl. Mater. Interfaces*, 2013, **5**, 1481.
20. M. Calvaresi, M. Quintana, P. Rudolf, F. Zerbetto and M. Prato, *ChemPhysChem*, 2013, **14**, 3447.
21. T. Fan, W. Zeng, Q. Niu, S. Tong, K. Cai, Y. Liu, W. Huang, Y. Min and A. J. Epstein, *Nanoscale Res. Lett.*, 2015, **10**:192.
22. W. Wan, Z. Zhao, H. Hu, X. Hao, T. C. Hughes, H. Ma, L. Pan and J. Qiu, *Carbon*, 2014, **76**, 46.
23. X. Li, Y. Zhang, T. Li, Q. Zhog, H. Li and J. Huang, *J. Power. Sources.*, 2014, **268**, 372.
24. W. Zhou, J. Liu, T. Chen, K. S. Tan, X. Jia, Z. Luo, Ch. Cong, H. Yang, C. M. Li and T. Yu, *Phys. Chem. Chem. Phys.*, 2011, **13**, 14462.
25. U. Mirsaidov, V. R. S. S. Mokkalpati, D. Bhattacharya, H. Andersen, M. Bosman, B. Özyilmaz and P. Matsudaira, *Lab Chip*, 2013, **13**, 2874.
26. T. Tojo, K. Fujisawa, H. Muramatsu, T. Hayashi, Y. A. Kim, M. Endo, M. Terrones and M. S. Dresselhaus, *RSC Adv.*, 2013, **3**, 4161.
27. D. Y. Hwang, J. Y. Yook and D. H. Suh, *RSC Adv.*, 2014, 35943.
28. V. R. Coluci, S. F. Braga, R. H. Baughman and D. S. Galvão, *Phys. Rev. B*, 2007, **75**: 125404.
29. G. mpourpakis, E. Tylianakis and G. E. Froudakis, *Nano Lett.*, 2007, **7**, 1893.
30. X. Shi, N. M. Pugno and H. Gao, *Acta. Mech. Solida. Sin.*, 2010, **23**, 484.

31. Z. Xu, B. Zheng, J. Chen and C. Gao, *Chem. Mater.*, 2014, **26**, 6811.
32. Y. Si, J. Yu, X. Tang, J. Ge and B. Ding, *Nat. Commun.*, 2014, **5**: 5802.
33. H. Sun, Z. Xu and C. Gao, *Adv. Mater.*, 2013, **25**, 2554.
34. Z. Xu and C. Gao, *ACS Nano*, 2011, **5**, 2908.
35. Z. Xu and C. Gao, *Nat. Commun.*, 2011, **2**: 571.
36. Z. Xu, H. Sun, X. Zhao and C. Gao, *Adv. Mater.*, 2013, **25**, 188.
37. L. Peng, Z. Xu, Z. Liu, Y. Wei, H. Sun, Z. Li, X. Zhao and C. Gao, *Nat. Commun.*, 2015, **6**:5716.
38. M. D. Stoller, S. Park, Y. Zhu, J. An and R. S. Ruoff, *Nano Lett.*, 2008, **8**, 3498.
39. J. R. Miller and P. Simon, *Science*, 2008, **321**, 651.
40. P. Simon and Y. Gogotsi, *Nat. Mater.*, 2008, **7**, 845.
41. Y. Wang, Z. Shi, Y. Huang, Y. Ma, C. Wang, M. Chen and Y. Chen, *J. Phys. Chem. C*, 2009, **113**, 13103.
42. Z. Lei, N. Christov and X. S. Zhao, *Energy Environ. Sci.*, 2011, **4**, 1866.
43. D. Yu and L. Dai, *J. Phys. Chem. Lett.*, 2010, **1**, 467.
44. J. Yan, Z. Fan, T. Wei, W. Qian, M. Zhang and F. Wei, *Carbon*, 2010, **48**, 3825.
45. Y. Zhu, S. Murali, M. D. Stoller, K. J. Ganesh, W. Cai, P. J. Ferreira, A. Pirkle, R. M. Wallace, K. A. Cychosz, M. Thommes, D. Su, E. A. Stach and R. S. Ruoff, *Science*, 2011, **332**, 1537.
46. M. F. El-Kady, V. Strong, S. Dubin and R. B. Kaner, *Science*, 2012, **335**, 1326.
47. S. Park, J. An, J. R. Potts, A. Velamakanni, S. Murali and R. S. Ruoff, *Carbon*, 2011, **49**, 3019.
48. K. Xie, X. Qin, X. Wang, Y. Wang, H. Tao, Q. Wu, L. Yang and Z. Hu, *Adv. Mater.*, 2012, **24**, 347.
49. F. Liu, S. Song, D. Xue and H. Zhang, *Adv. Mater.*, 2012, **24**, 1089.

50. X. Yang, J. Zhu, L. Qiu and D. Li, *Adv. Mater.*, 2011, **22**, 2833.
51. Z. Bo, W. Zhu, W. Ma, Z. Wen, X. Shuai, J. Chen, J. Yan, Z. Wang, K. Cen and X. Feng, *Adv. Mater.*, 2013, **25**, 5799.
52. X. Yang, C. Cheng, Y. Wang, L. Qiu and D. Li, *Science*, 2013, **341**, 534.
53. T. Huang, B. Zheng, Z. Liu, L. Kou and C. Gao, *J. Mater. Chem. A*, 2015, **3**, 1890.
54. Y. Yoon, K. Lee, C. Baik, H. Yoo, M. Min, Y. Park, S. Mi Lee and H. Lee, *Adv. Mater.*, 2013, **25**, 4437.

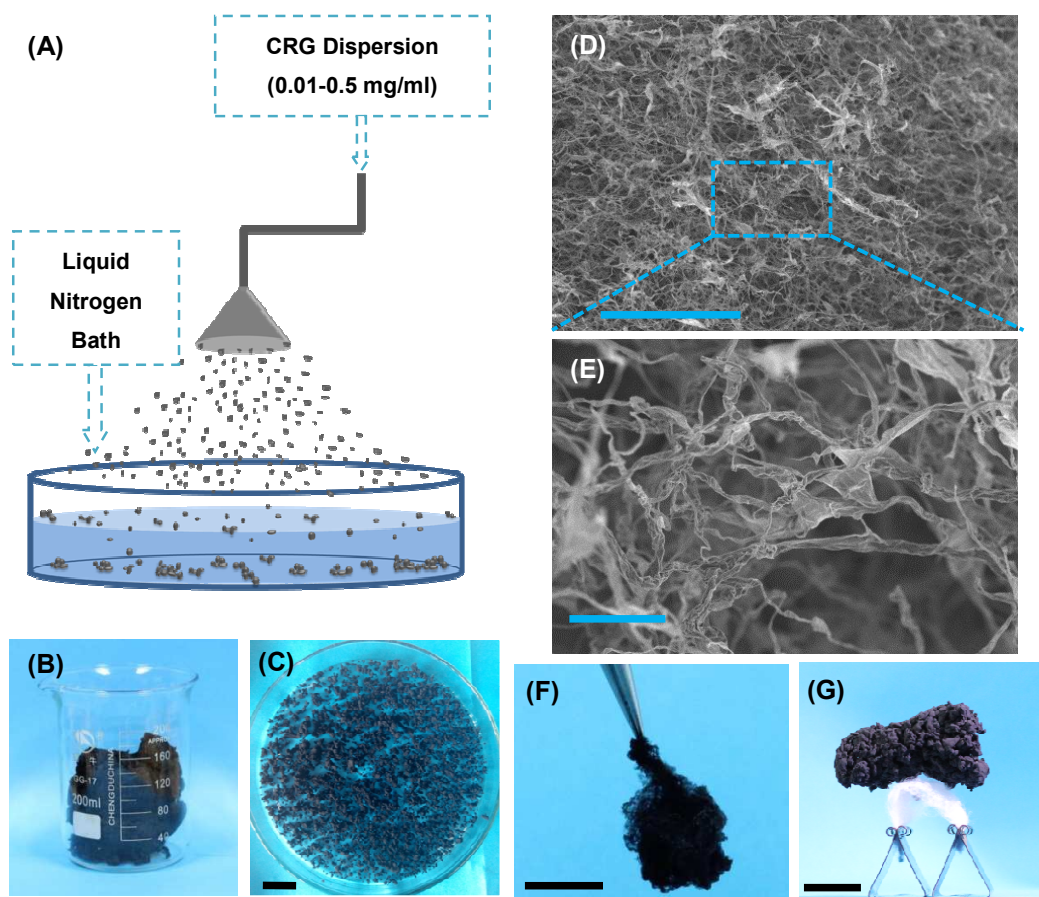


Figure 1 (A) Illustration of spray-freezing procedure; (B) and (C) Photo of GNS5, scale bar: 2 cm; (D) and (E) SEM images of GNS5, scale bar: 100 and 10  $\mu\text{m}$ ; (F) Photo of GNS1; (G) Photo of GNS2 comparing with cotton, scale bars: 1 cm.

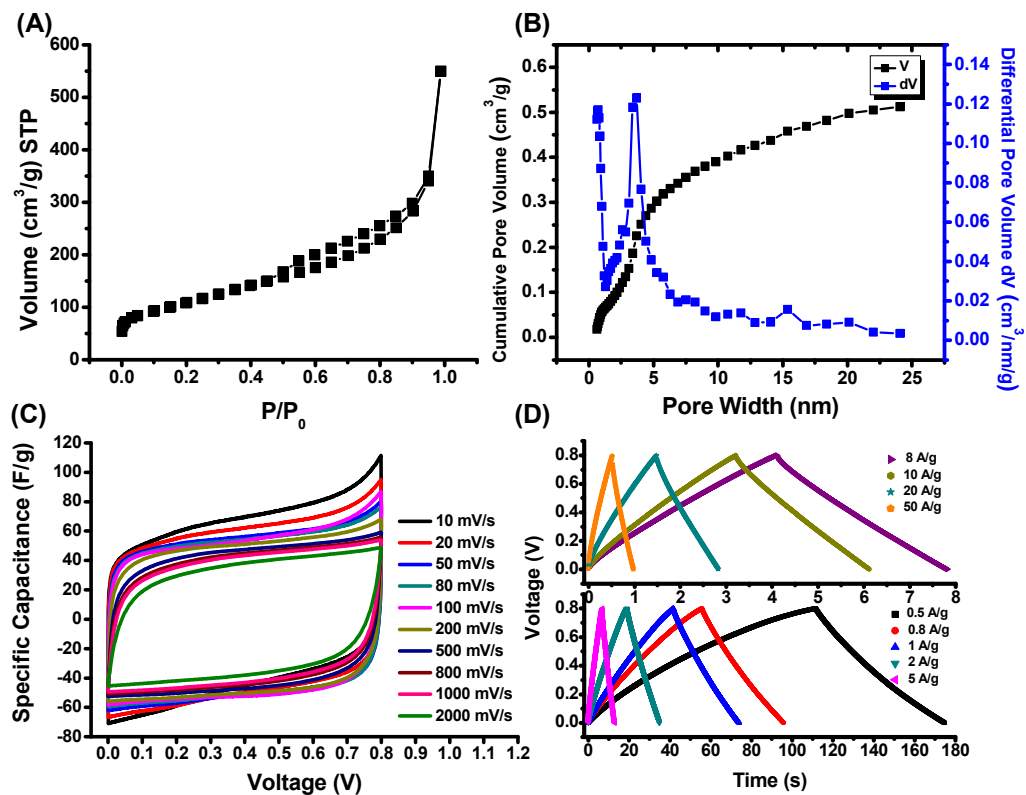


Figure 2 (A) High resolution, low pressure  $N_2$  isotherm of GNS4; (B) Cumulative pore volume and pore size distribution for  $N_2$  (using a slit pore QSDFT model) of GNS4; (C) CV curves of GNS2 in 1M  $H_2SO_4$ ; (D) GCD curves of GNS2 in 1M  $H_2SO_4$ .

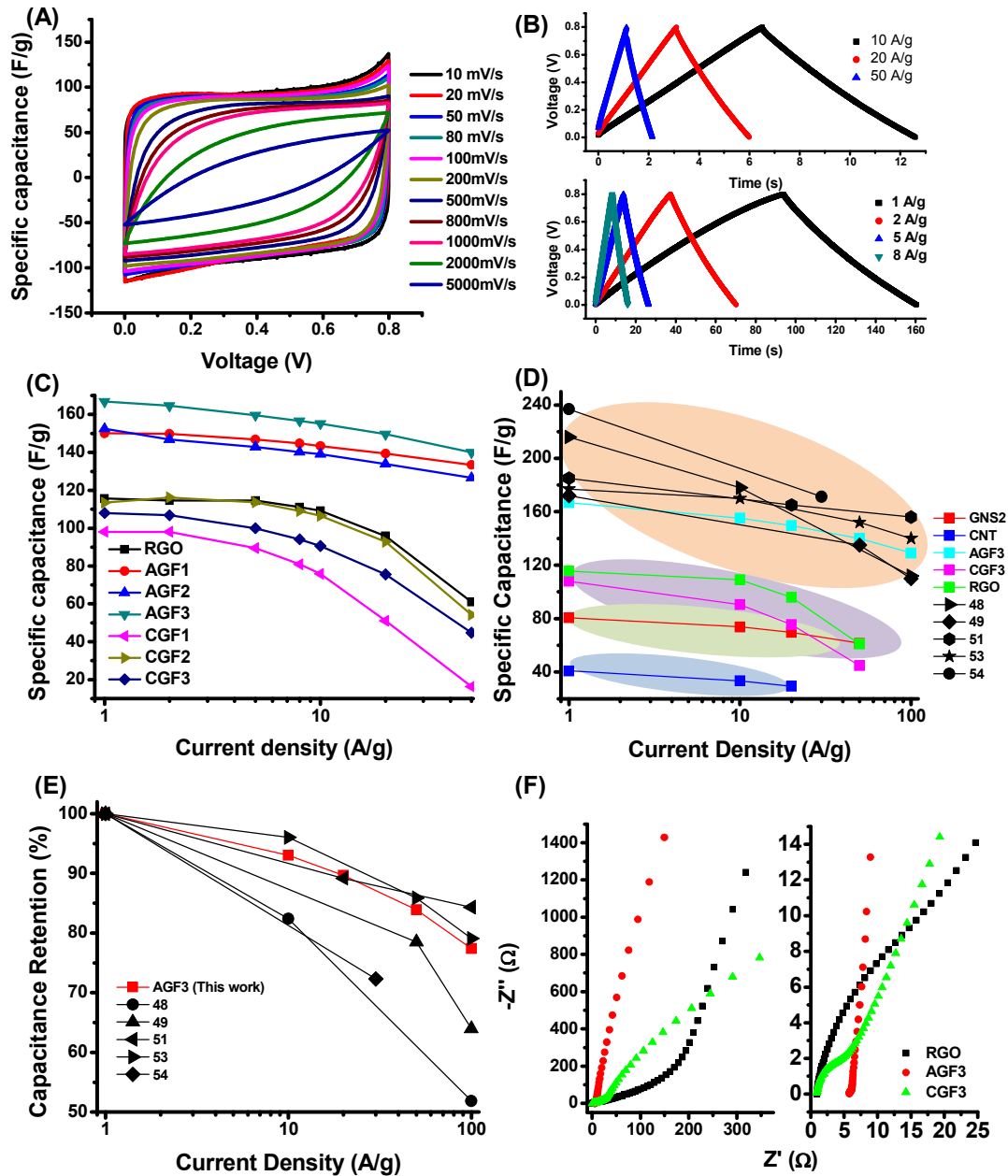


Figure 3 (A) CV curves of AGF3; (B) GCD curves of AGF3; (C) Electrochemical performances of different films characterized by GCD. (D) Specific capacitance comparison of this work with other related works; (E) Capacitance retention comparison of this work with other related works; (F) electrochemical impedance spectroscopy comparison of RGO film, AGF3 and CGF3; All the above tests were

conducted in aqueous electrolyte (1M H<sub>2</sub>SO<sub>4</sub>).

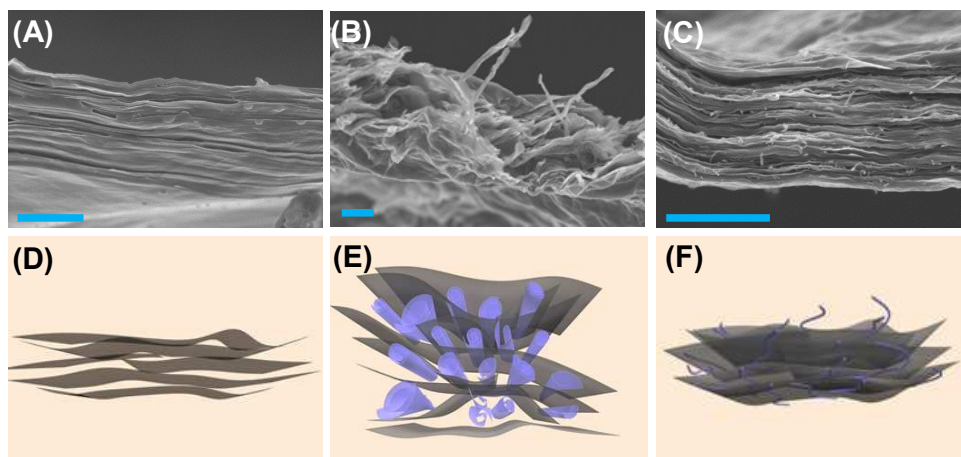


Figure 4 SEM image of RGO film (A), AGF3 (B) and CGF (C); Cartoon illustration of RGO film (D), AGF3 (E) and CGF (F), the scale bars in SEM images are 1  $\mu$ m.

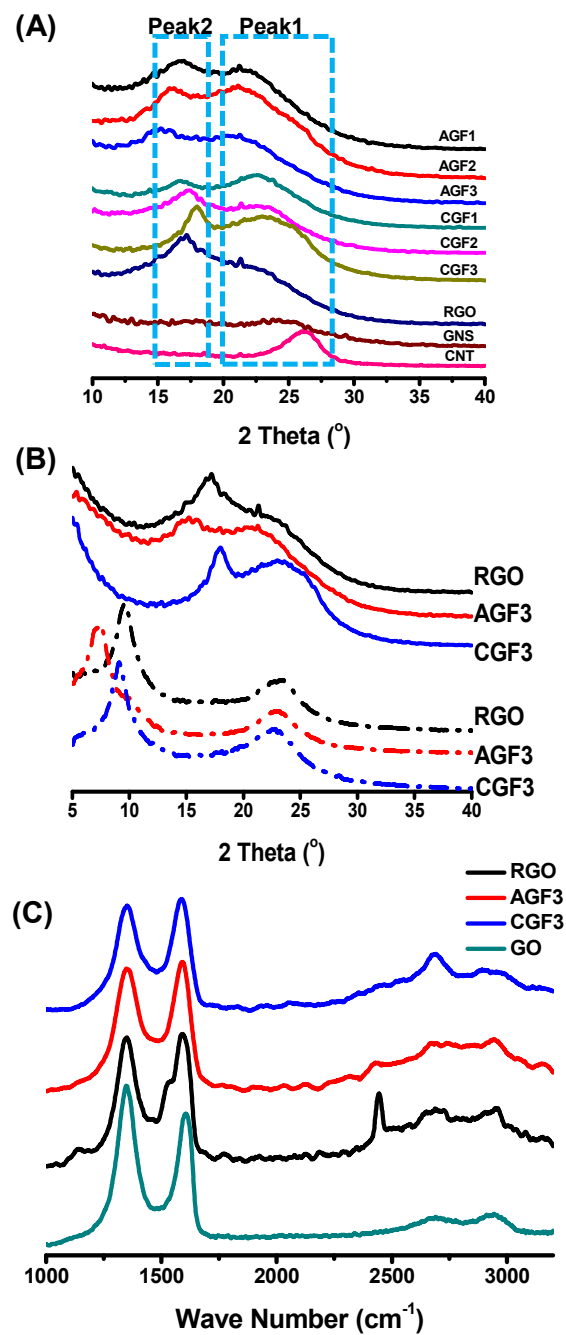


Figure 5 (A) XRD peaks of AGFs, CGFs, RGO films, GNS and CNT; (B) XRD peaks of dry films (solid lines) and wet films swollen by organic electrolyte (dash dot lines); (C) Raman spectra of RGO film, AGF3, CGF3 and GO.

**Table 1** XRD peaks and d-space of samples.

Name	Peak1 (°)	d <sub>1</sub> (Å)	Peak2 (°)	d <sub>2</sub> (Å)
AGF1	21.24	4.18	16.67	5.31
AGF2	21.14	4.20	15.89	5.57
AGF3	20.36	4.36	15.23	5.81
CGF1	22.65	3.92	16.73	5.30
CGF2	22.50	3.95	17.40	5.09
CGF3	22.99	3.87	17.99	4.93
RGO	22.36	3.97	17.21	5.15